nature biomedical engineering

ARTICLES

PUBLISHED: 13 MARCH 2017 | VOLUME: 1 | ARTICLE NUMBER: 0041

# A carbon nanotube reporter of microRNA hybridization events *in vivo*

Jackson D. Harvey[1,2], Prakrit V. Jena[1], Hanan A. Baker[1,2], Gül H. Zerze[3], Ryan M. Williams[1], Thomas V. Galassi[1,2], Daniel Roxbury[4], Jeetain Mittal[3] and Daniel A. Heller[1,2]*

**MicroRNAs and other small oligonucleotides in biofluids are promising disease biomarkers, yet conventional assays require complex processing steps that are unsuitable for point-of-care testing or for implantable or wearable sensors. Single-walled carbon nanotubes are an ideal material for implantable sensors, owing to their emission in the near-infrared spectral region, photostability and exquisite sensitivity. Here, we report an engineered carbon-nanotube-based sensor capable of real-time optical quantification of hybridization events of microRNA and other oligonucleotides. The mechanism of the sensor arises from competitive effects between displacement of both oligonucleotide charge groups and water from the nanotube surface, which result in a solvatochromism-like response. The sensor, which allows for detection via single-molecule sensor elements and for multiplexing by using multiple nanotube chiralities, can monitor toehold-based strand-displacement events, which reverse the sensor response and regenerate the sensor complex. We also show that the sensor functions in whole urine and serum, and can non-invasively measure DNA and microRNA after implantation in live mice.**

The detection of oligonucleotide hybridization is important for a broad range of applications, from devices based on dynamic DNA nanotechnology to clinical point-of-care diagnostics. Oligonucleotides in biofluids, such as serum, urine and peritoneal fluid[1,2], are a promising source of biomarkers for a variety of pathologies, including cancer[3,4]. Of the potential biomarker oligonucleotides[5–7], microRNA (miRNA) is highly stable in body fluids, and many studies have identified specific patterns of miRNA expression indicative of disease states[3,8–13]. Devices that can measure changes in biomarker miRNA[14] or cell-free DNA[15] concentrations in biofluids such as urine, serum or ascitic fluid in patients with risk factors for a disease or its relapse may improve early detection and treatment. Implantable or wearable devices that enable minimally invasive continuous biomarker monitoring may extend this strategy to detect biomarkers at the earliest possible stages of disease.

The current standard for miRNA measurement, with limits of detection ranging from attomolar to femtomolar[16], is quantitative PCR (qPCR)[17], but this method requires purification and amplification of miRNA that can introduce biases and variability[18]. Commercially available techniques that do not involve amplification, such as microarrays, suffer from poorer sensitivity (picomolar to nanomolar) and high false-positive rates[16,18]. Detection strategies that avoid amplification, labelling and purification from biofluids are under investigation[19,20], but *in vivo* detection strategies are sparse. The detection of nucleic acid biomarkers in real-time and *in situ* within living tissues and organisms remains an important challenge.

Of the potential materials for detecting nucleic acids, individually dispersed semiconducting single-walled carbon nanotubes (SWCNTs) exhibit exciting properties for use as optical biomedical sensors[21,22]. Semiconducting carbon nanotubes do not photobleach[23] and they are fluorescent in the near-infrared spectral region[24], a range of wavelengths that maximally penetrate tissue[25]. Their emission wavelength[26] and intensity[27] are sensitive to the local environment, allowing perturbations at the nanotube surface to be transduced via modulation of their emission, with up to single-molecule sensitivity[28]. Up to 17 distinct nanotube (*n*,*m*) species (chiralities) with unique and resolvable emission wavelengths can be measured, thereby allowing for multiplexed detection schemes[29].

Here, we describe a label-free approach to detect hybridization events of miRNA and other oligonucleotides transiently and *in vivo*. We designed a sensor that transduces the hybridization of small DNA and RNA oligonucleotides into spectral changes of carbon nanotube photoluminescence, and determined its mechanism of action via experiments and molecular dynamics simulations to be a competitive response to local dielectric and electrostatic factors. Using this understanding, we designed a scheme wherein amphiphilic moieties undergo triggered assembly on the nanotube surface upon binding of target miRNA, resulting in a markedly enhanced spectral response. We show that the sensor enables multiplexed detection using different nanotube chiralities and real-time monitoring of toehold-mediated DNA-strand displacement, which causes a reversal of the signal response. The sensor is highly resistant to non-specific interactions with biological molecules, allowing for direct detection in urine and serum. Finally, we demonstrate the first *in vivo* optical detection of target DNA and miRNA by encasing the sensor in an implantable device through which we non-invasively detect hybridization in live mice via near-infrared fluorescence.

## Results and discussion

**Development of the sensor.** We synthesized a DNA–nanotube complex consisting of a single oligonucleotide sequence with two domains—one to impart nanotube colloidal stability (nanotube-binding sequence) and a second with a sequence complementary to a target oligonucleotide (miRNA capture sequence). For the miRNA capture sequence, we chose a specific 23-mer miRNA, miR-19, as a

[1]Molecular Pharmacology Program, Memorial Sloan Kettering Cancer Center, New York, New York 10065, USA. [2]Department of Pharmacology, Weill Cornell Medical College, New York, New York 10065, USA. [3]Department of Chemical and Biomolecular Engineering, Lehigh University, Bethlehem, Pennsylvania 18015, USA. [4]Department of Chemical Engineering, University of Rhode Island, Kingston, Rhode Island 02881, USA. *e-mail: hellerd@mskcc.org

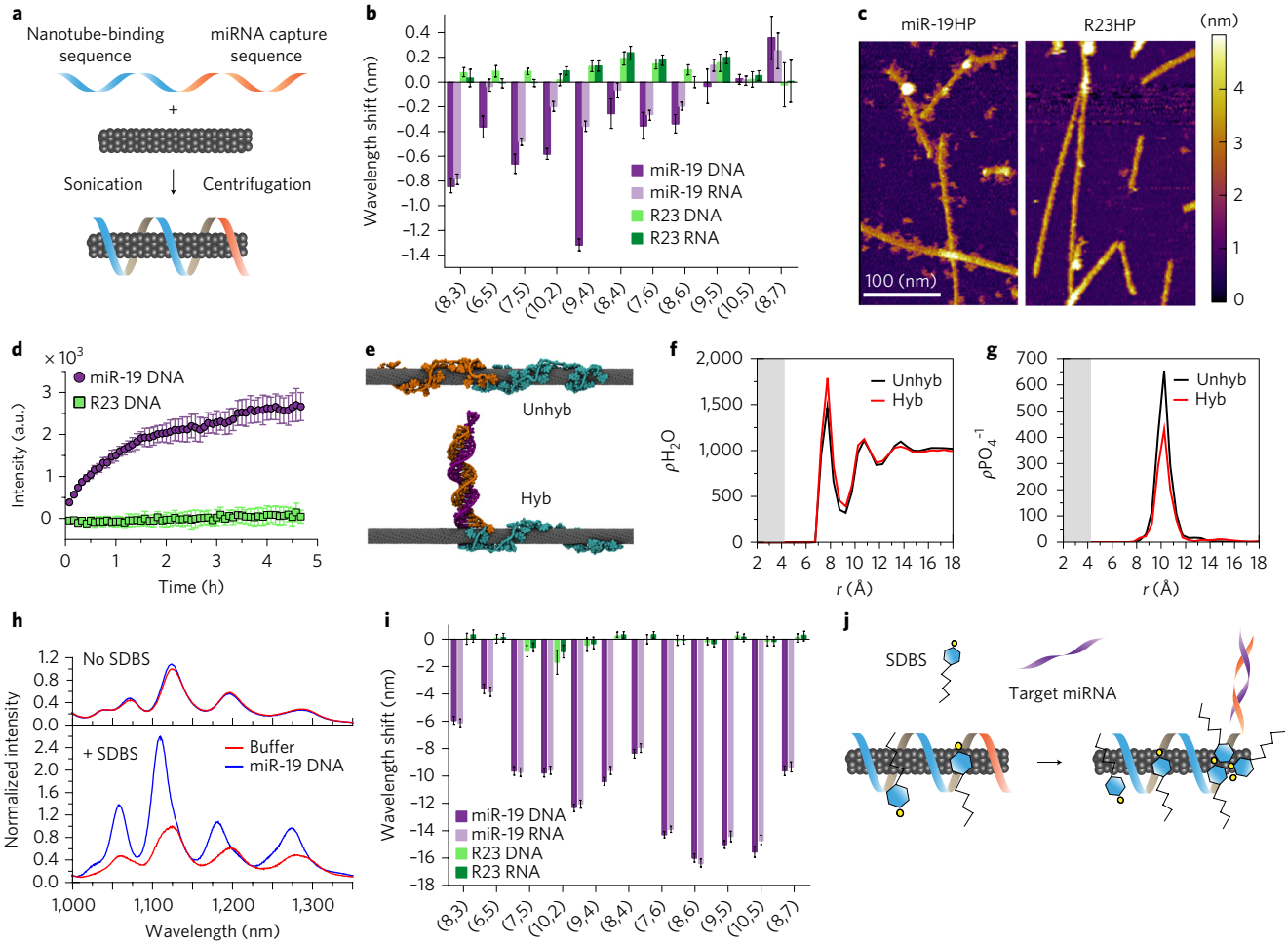


**Figure 1 | Carbon nanotube sensor for the detection of miRNA hybridization events. a**, Construction scheme of the miRNA sensor complex, consisting of a single DNA oligonucleotide containing a nanotube-binding sequence (blue) and a miRNA capture sequence (orange) that is non-covalently bound to the carbon nanotube surface. **b**, Response of the GT15mir19 sensor to analyte DNA or RNA with the miR-19 sequence or a control sequence (R23), for each nanotube chirality (*n*,*m*). A positive wavelength shift denotes a red-shift in the emission peak, and negative values denote a blue-shift. **c**, AFM images of the sensor complex on incubation with non-complementary (R23HP) or complementary (miR-19HP) hairpin DNA. **d**, Intensity of Cy5 emission (in arbitrary units, a.u.) from the GT15mir19-Cy5–nanotube complex after introducing miR-19 DNA or R23 DNA. **e**, Snapshot images of molecular dynamics simulations of the GT15mir19 sensor (Unhyb) and GT15mir19 sensor hybridized with miR-19 (Hyb) after equilibrating for 250 ns. Blue-green colour denotes the $(GT)_{15}$ nanotube-binding sequence, and orange denotes the miR-19 capture sequence. The purple strand denotes miR-19. **f**. Density ($\rho$) of water as a function of radial distance from the nanotube, calculated for both simulations. **g**, Density ($\rho$) of phosphate groups as a function of radial distance from the nanotube, calculated for the final frame of both simulations. Grey shaded region represents area occupied by the nanotube. **h**, Photoluminescence spectra of the GT15mir19 sensor on hybridization with miR-19 in the absence (top) or presence (bottom) of SDBS; intensity normalized to the buffer condition. **i**, Response of the sensor complex to analyte DNA or RNA with the miR-19 sequence, or a control sequence (R23), in the presence of SDBS, for each nanotube chirality. **j**, Cartoon depicting the proposed mechanism of SDBS-mediated enhancement of the blue-shift response to hybridization. All error bars represent the standard deviation for three technical replicates.

model target due to its role in oncogenesis[30]. Figure 1a shows the synthesis scheme. A screen of potential nanotube-binding sequences found that $(GT)_{15}$, which is known to efficiently encapsulate nanotubes[31], provided superior resistance to non-complementary oligonucleotides (Supplementary Fig. 1). The purified DNA–nanotube construct was found to be highly photoluminescent and is henceforth referred to as the GT15mir19 sensor.

The optical response of the GT15mir19 sensor was then tested using both a DNA-based and RNA-based analyte miR-19 sequence, as well as a length-matched, randomly generated, non-complementary control (R23). After incubation with miR-19 or R23, 11 different nanotube chiralities were measured via two-dimensional excitation/emission photoluminescence spectroscopy[32] ('PL plots'; Supplementary Fig. 2). Each nanotube emission peak exhibited a shift in wavelength that was specific to the miR-19 target sequence over the R23 control (Fig. 1b). In general, on introduction of the target oligonucleotide, the nanotube emission peak was blue-shifted and its magnitude increased (Supplementary Fig. 3); excitation peaks ($E_{22}$ transitions) were also blue-shifted (Supplementary Fig. 4).

To verify that hybridization to the GT15mir19 sensor occurred on introduction of the target, we designed a hairpin oligonucleotide that would make binding of the target more apparent by atomic force microscopy (AFM). The oligonucleotide was composed of the miR-19 or R23 sequence, a short spacer and a 52-nucleotide hairpin region (diagram in Supplementary Fig. 5). After incubation with the miR-19 hairpin, the average height of the sample increased by ~0.6 nm, as measured by AFM in dry conditions (Supplementary Fig. 5). On imaging in aqueous conditions, we observed distinct protrusions from the nanotubes that were absent in the R23 hairpin-treated sample and buffer controls (Fig. 1c and Supplementary

Fig. 6). On the basis of this pattern and other AFM studies[33], we estimate that the GT15mir19 sensor presents 5–10 binding sites per 100 nm of nanotube. Our preparation method yielded nanotubes with a mean length of 166 nm (s.d. 149 nm)[34]; thus, we calculated that an average single nanotube could potentially bind approximately 8–17 copies of miRNA.

Because the mechanism of nanotube spectral changes induced by oligonucleotide hybridization is poorly understood, we designed a set of experiments to better understand the structural changes of the sensor induced by hybridization. We first investigated whether the hybridized duplex remained near the nanotube surface after the binding of target miRNA. We developed an assay using an organic fluorophore conjugated to the miRNA capture sequence under the premise that the fluorophore intensity would increase on hybridization if the fluorophore desorbed from the nanotube surface, as organic fluorophores are known to be quenched on interaction with the nanotube surface via an energy transfer mechanism[35]. We suspended nanotubes with the GT6mir19 DNA sequence (shortened due to synthesis constraints), which included the Cy5 dye conjugated to the 3′ end of the miR-19-binding domain (scheme in Supplementary Fig. 7). On addition of miR-19 to the modified complex, we found that Cy5 fluorescence increased over time, while the R23 sequence caused no change in Cy5 fluorescence (Fig. 1d). To validate GT6mir19-Cy5 as a proxy for the GT15mir19 sequence, we measured the nanotube emission on introduction of the miR-19 sequence to the fluorophore-labelled complex. Again, we saw blue-shifting on hybridization with the target oligonucleotide, suggesting the same sensor function despite the shortened nanotube-binding domain (Supplementary Fig. 8). In agreement with the Cy5 fluorescence change, we found that nanotube fluorescence emission was blue-shifted at a slower rate versus GT6mir19 without Cy5. (Supplementary Fig. 8). We interpret this relatively slow rate as being a result of the affinity of Cy5 for the nanotube surface based on $\pi$-stacking interactions between the Cy5 dye (rich in $\pi$ electrons) and the graphitic $\pi$ electrons of the nanotube. The fluorophore de-quenching and AFM together suggest a final hybridized structure consisting of a partial duplex dissociating from the nanotube surface.

Using all-atom molecular dynamics simulations, we assessed whether the GT15mir19 sequence could remain stable on the nanotube after partial hybridization. The pre-hybridized sequence was placed in the vicinity of the (9,4) nanotube with explicit water and counterions, and a simulation was run for 250 ns (see Methods for details). The single-stranded portion of the oligomer bound to the nanotube and the hybridized construct remained stable on the nanotube surface for the remainder of the simulation (Fig. 1e, 'Hyb'; Supplementary Video 1). A second simulation was run without the hybridization strand and in this case, the entire oligomer bound to the surface and wrapped the nanotube, with the nucleobases located close to the nanotube surface in a parallel orientation (Fig. 1e, 'Unhyb'; Supplementary Video 2).

The simulations allowed the quantification of nucleobase adsorption to the nanotube surface. We measured the radial distance of the nucleobases from the nanotube surface and their stacking angles relative to the nanotube surface (Supplementary Fig. 9). We observed that, in the case of the hybridized complex, all bases of the $(GT)_{15}$ nanotube-binding domain remained adsorbed on the nanotube surface, whereas only one or two terminal bases of the double-stranded miR-19/miRNA capture sequence adsorbed to the nanotube surface. In the simulation without the complementary strand, all bases of the $(GT)_{15}$ nanotube binding domain adsorbed to the nanotube surface, as well as most of the bases of the miR-19 miRNA capture sequence (Supplementary Fig. 9).

We assessed the thermodynamic concerns regarding the stability of the hybridized duplex in the presence of the nanotube. Molecular dynamics simulations of hybridized miR-19, without the $(GT)_{15}$ nanotube binding domain, in the presence of the nanotube were run using several different initial conditions (Supplementary Fig. 10 and Supplementary Video 3). In all simulations, no de-hybridization of the duplex was observed, suggesting that the nanotube would not destabilize the hybridized duplex. To understand how the partially hybridized state of the DNA is stable on the nanotube (or preferred over single-strand adsorption on the nanotube), we conducted a free energy analysis (Supplementary Text and Supplementary Fig. 11). The analysis suggests that hybridization of the double-stranded DNA is favoured if the analyte strand is not initially adsorbed on the nanotube surface, as is the case in our experiments.

We also analysed the molecular dynamics simulations to gain a quantitative understanding of the carbon nanotube spectral response to hybridization. Comparing the water density as a function of radial distance from the nanotube at the end of the two simulations, we found a slight increase in the water concentration near the nanotube in the hybridized structure (Fig. 1f). In addition, we found that the density of phosphate groups as a function of distance from the nanotube decreased on hybridization (Fig. 1g). While an increase in local water density is known to cause red-shifting[36] of the nanotube emission wavelength, recent research[34] has found that a decrease in local anionic charge density in the local environment of the nanotube causes a blue-shift. As the nanotube emission exhibited a net blue-shift on hybridization, we thus conclude that the effect of the removal of phosphate charges from the nanotube surface out-competed the effects of increased local water density.

As the simulations showed an increase in available nanotube surface area on hybridization, we hypothesized that additional small amphipathic molecules might assemble on this newly exposed nanotube surface to enhance the optical response. Low concentrations of several candidate surfactants (Supplementary Table 1) were tested to determine whether they changed the optical response of the GT15mir19 sensor (Supplementary Text and Supplementary Figs 12 and 13). The study found that a low concentration (0.2% w/v or 5.7 mM) of sodium dodecylbenzenesulfonate (SDBS), a mild surfactant known to associate with nanotubes[37], resulted in an increase in the degree of hybridization-dependent blue-shifting and intensity enhancement by an order of magnitude (Fig. 1h). In the SDBS-supplemented buffer-only condition and in the presence of the R23 control, the emission bands broadened slightly but did not increase or shift appreciably. On hybridization in the presence of SDBS, all nanotube chiralities exhibited a greatly enhanced blue-shift (Fig. 1i and Supplementary Figs 14–17), even those that were not blue-shifted in the absence of SDBS (Fig. 1b). A significant blue-shift in the excitation wavelength was also observed (Supplementary Fig. 15). The magnitude of blue-shifting and intensity enhancement (Supplementary Fig. 16) on hybridization of DNA and RNA were identical. In the

**Table 1 | Disease-relevant miRNA biomarkers.**

| Name | Disease relevance | Biofluid | Reference |
|---|---|---|---|
| miR-21 | Diffuse large B-cell lymphoma | Serum | 9 |
| miR-96 | Urothelial carcinoma | Urine sediment | 10 |
| miR-183 | Urothelial carcinoma | Urine sediment | 10 |
| miR-126 | Urinary bladder cancer | Voided urine | 11 |
| miR-182 | Urinary bladder cancer | Voided urine | 12 |
| miR-152 | Healthy control | Voided urine | 11 |
| miR-494 | Acute kidney injury | Voided urine | 13 |
| miR-509 | Healthy control, highly expressed | Voided urine | 8 |
| miR-39 | Found only in *C. elegans*; spike-in control | N/A | 3 |

N/A, not applicable.

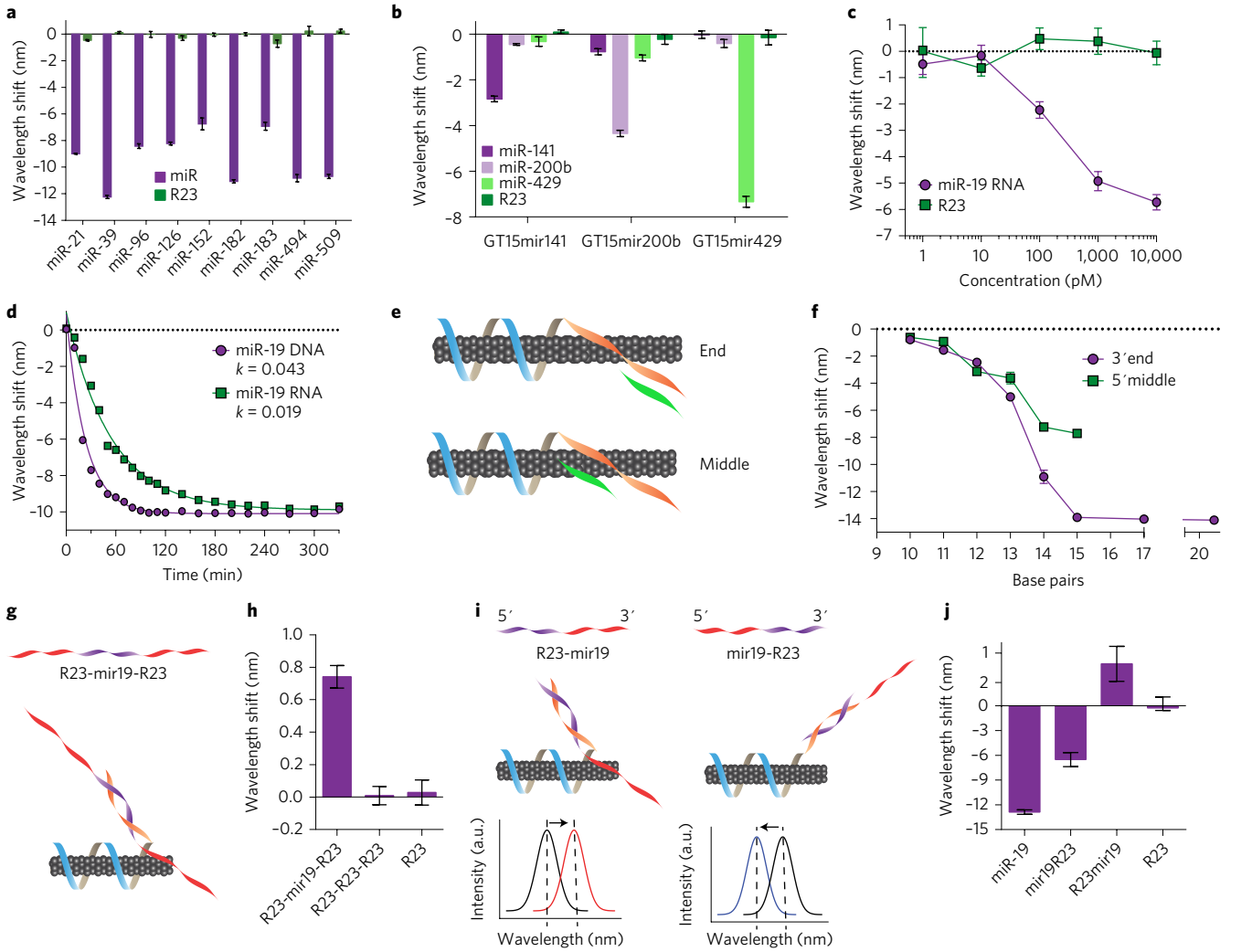


**Figure 2 | Characterization of miRNA detection limit, kinetics and functionality. a**, Optical responses of nanotube sensors ((7,5) nanotube species), each with a different capture sequence to recognize the specified miRNA sequence (DNA analogue). **b**, Spectral responses (blue-shifts) of nanotube sensors ((9,4) nanotube species), with specified capture sequences, to related miR-200 family sequences (miR-141, 5′-TAACACTGTCTGGTAAAGATGG-3′; miR-200b, 5′-TAA**T**ACTG**C**CTGGTAA**T**GATG**A**-3′; miR-429, 5′-TAA**T**ACTGTCTGGTAAA**ACC**G**T**-3′; differences versus miR-141 are indicated by bold font). **c**, Dose–response curve of the GT15mir19 sensor ((7,6) nanotube). **d**, Kinetics of the sensor response to miR-19 RNA or the DNA analogue, fitted with the exponential function $y = y_0 e^{-kt}$; where $y$ is the wavelength shift, $y_0$ is the original wavelength shift, $k$ is rate constant and $t$ is time. The coefficient of determination ($R^2$) was 0.97 and 0.99 for DNA and RNA, respectively. **e**, Cartoon illustrating truncated analyte (green) sequences (5′-(GT)15--TCAGTTTTGCATAGATTTGCACA-3′; 3′-CTAAACGTGT-5′; 5′-(GT)15--TCAGTTTTGCATAGATTTGCACA-3′; 3′-AGTCAAAACG-5′) complementary to the middle or 3′ end of the capture (orange) sequence. **f**, Emission response of the sensor to a series of truncated sequences (length specified in the *x* axis) designed to hybridize to either the middle or 3′ end of the capture sequence. **g**, Cartoon illustrating a modified analyte sequence and expected configuration on binding to the GT15mir19 sensor. **h**, Spectral response of the GT15mir19 sensor ((8,6) nanotube) to interactions with long analyte sequences. **i**, Cartoons depicting an experiment designed to assess orientation of partially complementary sequences, including predicted sensor responses. **j**, Response of (8,6) nanotubes on interrogation of the GT15mir19 sensor with partially complementary oligonucleotides. All error bars represent the standard deviation for three technical replicates.

absence of the target oligonucleotide, the GT15mir19 sensor emission remained stable over a wide range of SDBS concentrations (Supplementary Fig. 17). We present our model of SDBS-mediated hybridization-dependent signal enhancement in Fig. 1j, wherein hybridization triggers SDBS assembly on the newly exposed nanotube surface. For a more detailed analysis of the observed spectroscopic changes induced by SDBS, see the Supplementary Text.

To further assess the specificity of the sensor response, we introduced an ensemble of randomly generated oligonucleotides. A random library of 23-nucleotide oligonucleotides, with a diversity of approximately $4^{23}$ different sequences, was introduced to the GT15mir19 sensor, resulting in no response (Supplementary Fig. 19). In the presence of the random library, the GT15mir19 sensor maintained sensitivity to miR-19.

**Detection limit, kinetics and breadth of applicability.** Given the variety of potential miRNA biomarkers, we sought to assess the modularity of the sensor. The miRNA capture sequence was substituted with several sequences specific to nine different serum or urine miRNA biomarkers, as well as a sequence not found in humans (*Caenorhabditis elegans* miR-39) used for standardization in clinical applications[38] (Table 1). Each GT15mirX sensor was treated with SDBS and interrogated with its respective miRNA target sequence, which resulted in a wavelength shift compa-

rable to that of the original miR-19 sensor, with slight sequence-to-sequence variations (Fig. 2a and Supplementary Fig. 20). Intensity was similarly enhanced (Supplementary Fig. 21). In all of the sensors, no appreciable responses from the control sequence (R23) were observed.

To determine whether the SDBS-GT15mirX sensor could discriminate among similar sequences, three related sequences from the miR-200 family were selected. The miR-200 family plays an essential role in the epithelial-to-mesenchymal transition[39] in cancer. Focusing on the wavelength response of the (9,4) nanotube chirality, we observed a high degree of discrimination between the three sequences after 1 h of incubation (Fig. 2b). Complete time-course data for both the (9,4) and (8,6) nanotubes (Supplementary Figs 22 and 23, respectively) revealed that the intensity increase provided near perfect discrimination in most cases. Although the SDBS-GT15mirX sensor responded to target miRNA via both wavelength shifts and intensity changes, we assessed detection limits, kinetics and other sensor characteristics using the wavelength shift, due to the inherent quantifiability and internal standard provided by this mode.

To determine the limit and range of detection, a dose–response curve for the sensor was generated using a range of miR-19 concentrations spread over several orders of magnitude. At a minimal sensor concentration of 0.02 mg l$^{-1}$, the limit for detection of miRNA was between 10 and 100 pM (0.5–5 fmol) (Fig. 2c). Signal saturation occurred at a high concentration between 1 and 10 nM. The dynamic range was tuned by adjusting the concentration of the GT15mir19 sensor to cover at least five orders of magnitude, from 10 pM to 1 μM (Supplementary Fig. 24). We calculated the number of binding sites via the mass of DNA used to suspend 1 mg of nanotubes (see Methods). We estimated that 2.117 nM of miR-19 binding sites were available in a solution of 0.02 mg l$^{-1}$ of the GT15mir19 sensor, consistent with the observed saturating range of concentrations (between 1 and 10 nM).

The kinetics of both DNA and miRNA detection were assessed via transient measurements. The kinetics of 11 different nanotube chiralities were measured by excitation/emission spectroscopy (Supplementary Fig. 25). Within 10 min of introducing the analyte to the sensor, a significant blue-shift was observed. The rate of blue-shifting exhibited pseudo-first order kinetics and showed no obvious dependence on nanotube structure (Supplementary Fig. 26). The sensor kinetics were consistently faster for DNA versus RNA (×1.8 on average; Fig. 2d). We ascribe this difference to the longer persistence length and higher rigidity of single-stranded RNA, compared with single-stranded DNA[40].

To test whether the composition of the miRNA capture sequence influenced the sensor kinetics, we compared the response rates for the sensor using eight different miRNA capture sequences (Supplementary Fig. 27). On comparing the sensor kinetics as a function of guanine content, we found a significant correlation, with Pearson coefficients of −0.74195 ($P=0.035$) for the (9,4) nanotube and −0.77215 ($P=0.0248$) for the (8,6) nanotube (Supplementary Fig. 28). This result may be explained by the comparatively high affinity of guanine for the nanotube surface (G > A > T > C), which was determined previously via both molecular dynamics and *ab initio* calculations[41]. Thus, the affinity of guanine for the nanotube surface may slow the hybridization process. The content of other nucleotide bases, as well as the Gibbs free energy ($\Delta G$) associated with hybridization, did not show any statistically significant correlations (Supplementary Figs 29 and 30).

To better understand how the length of the target oligonucleotide and thermodynamics of hybridization relate to the optical response of the nanotube, we conducted several experiments using modified analyte oligonucleotides. We interrogated the G15mir19 sensor using analyte sequences between 10 and 23 nucleotides long that were complementary to either the 3′ end of the miRNA capture sequence, or the middle of the sequence, as depicted in Fig. 2e. We found that, in general, a shorter analyte sequence resulted in a smaller blue-shift of the nanotube emission, down to ~10 nucleotides, where there was virtually no response (Fig. 2f). In addition, the magnitude of the blue-shift response was consistently smaller when the analyte sequence was designed to hybridize to the middle of the capture sequence. This difference may be explained by the affinity of the capture sequence to the nanotube, as suggested by the results of the fluorophore quenching experiment, molecular dynamics (MD) simulations and free energy analyses[41].

To assess its broad applicability for the detection of different nucleic acid types, we assessed whether the sensor could detect oligonucleotides longer than miRNA sequences. First, we assessed how the GT15mir19 sensor would respond to a long oligonucleotide designed to contain a complementary sequence flanked by non-complementary sequences (Fig. 2g). When the sensor was interrogated with R23-mir19-R23, a 69-base-pair oligonucleotide with 23 complementary bases in the middle of the sequence, its emission was red-shifted—opposite of the expected blue-shift—even in the presence of SDBS (Fig. 2h, shown for (8,6) chirality). We therefore hypothesized that, when R23-mir19-R23 hybridizes to the recognition sequence, the R23 portion at the 5′ end may disrupt the sensor function by increasing the phosphate content near the nanotube surface to cause a red-shift of the nanotube emission. To test this hypothesis, we designed two long oligonucleotide sequences, R23-mir19 and mir19-R23, placing the R23 portion at either the 3′ end or 5′ end. The proposed orientation on binding and the predicted spectral shifts are shown in Fig. 2i—the two sensors were hypothesized to give the opposite spectral responses. The R23-mir19 oligonucleotide produced a red-shift, and the mir19-R23 oligonucleotide produced a blue-shift, as predicted (Fig. 2j). The magnitude of the blue-shift in response to mir19-R23 was smaller than that produced by the miR-19 control, suggesting that the unhybridized single-stranded nucleotides may bind to the nanotube surface, thereby diminishing the shift. This hypothesis warrants further study. Regardless, we conclude that sensors based on the GT15 nanotube binding domain and a general capture sequence can be extended to detect longer nucleic acid sequences, but the orientation of the oligonucleotide is critical for eliciting a desired spectral response.

**Measurements with single sensor complexes.** We assessed the sensor function on the single-nanotube level via spectral imaging. The sensor was deposited on a lysine-coated glass surface with sodium dodecyl sulfate (SDS). We then used hyperspectral microscopy[29] to spectroscopically image (9,4) nanotubes (Fig. 3a). Blue-shifting of single nanotubes was apparent on interrogation of the sensor with miR-19 RNA, but not with R23 RNA (Fig. 3b–d and Supplementary Fig. 31). Using the number of binding sites per unit of nanotube length (determined from AFM measurements; Fig. 1c), we attempted to estimate the number of copies of miRNA detected per nanotube. Because a diffraction-limited spot could contain a nanotube up to ~600 nm long[42], we estimate that the detection range was 1–60 miRNA molecules.

**Sensor multiplexing.** We assessed the potential for the multiplexed detection of several miRNA sequences via the use of different nanotube chiralities. Two nanotube preparations enriched for different nanotube chiralities were suspended with binding sequences for either miR-19 or miR-509. A preparation enriched in large-diameter species (Nano-C APT-200) was suspended with the GT15mir19 sequence, and a CoMoCAT preparation enriched in small-diameter species was suspended with the GT15mir509 sequence. Excitation/emission plots showed that the GT15mir19 sensor, encapsulating the APT-200 nanotubes, effectively lacked the (6,5) species (Fig. 4a), while the GT15mir509 sensor, encapsulating the small-diameter

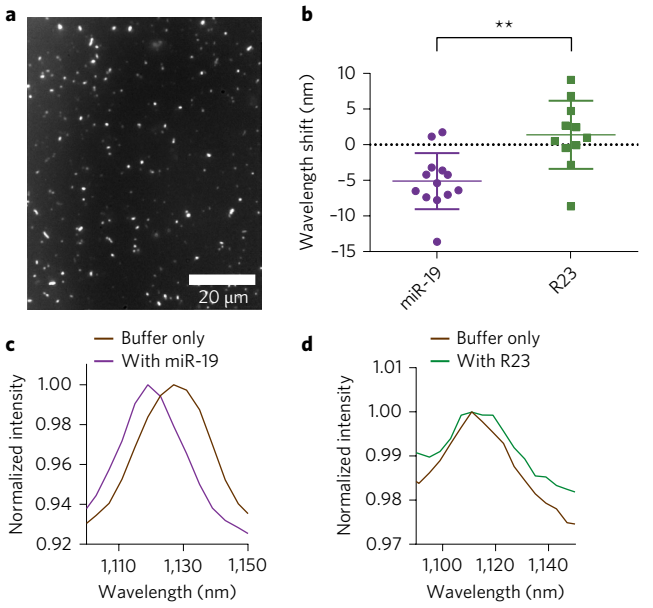


**Figure 3 | Single-nanotube response to miRNA hybridization.** **a**, Broadband near-infrared image of the GT15mir19 sensor adsorbed to a glass surface. **b**, Change in emission wavelength of individual (9,4) nanotubes after incubation of the surface-bound complexes with miR-19 RNA or R23 RNA at room temperature. $^{**}P = 0.0014$ (unpaired two-tailed *t*-test; $n = 24$). Error bars, mean ± s.d. **c**,**d**, Representative spectra of the same sensor complex in buffer only and 50 min after introducing miR-19 (**c**) and the R23 control sequence (**d**).

enriched CoMoCAT preparation, lacked the (8,6) species (Fig. 4b). Absorbance spectra verified the differential enrichment of nanotube chiralities between these samples (Supplementary Fig. 32). After mixing the two nanotube preparations, each miRNA sequence added individually was recognized by the appropriate nanotube chirality (Fig. 4c). When miR-19 and miR-509 were added together, the spectral shift was almost identical to that seen when either miRNA was added alone.

**Toehold-mediated strand displacement.** We examined whether the spectral response of the sensor could be reversed via toehold-mediated strand displacement. Strand displacement reactions occur through the use of 'toeholds,' single-strand overhangs on duplexed DNA that facilitate binding of a complementary strand, which is thermodynamically favoured due to complete complementarity, and is thus able to displace the shorter bound strand[43]. We truncated the miRNA capture sequence of the GT15mir19 sensor to leave a six nucleotide overhang[44] after hybridization with the target strand to test whether the addition of a removing strand to bind the toehold and displace the target would reverse the spectral shift, according to the proposed scheme in Fig. 5a. On addition of miR-19 to the modified GT15mir19 sensor, the nanotube emission blue-shifted and the intensity increased as expected (Fig. 5b,c). After 5 h, the removing strand was added, at which point the blue-shifting ceased and the emission began to undergo a steady red-shift (Fig. 5b). The emission intensity exhibited a similar reversal (Fig. 5c). We note that the signal reversal was slower than detection in the forward direction, which is probably due to the energetic barrier for the truncated capture sequence to displace SDBS from the nanotube surface.

**Detection of miRNA in biofluids.** We assessed the ability of the GT15mir19 sensor to detect miRNA binding events in common biofluids—urine and serum—due to their clinical value as sources of miRNA biomarkers[8]. The GT15mir19 sensor and SDBS were

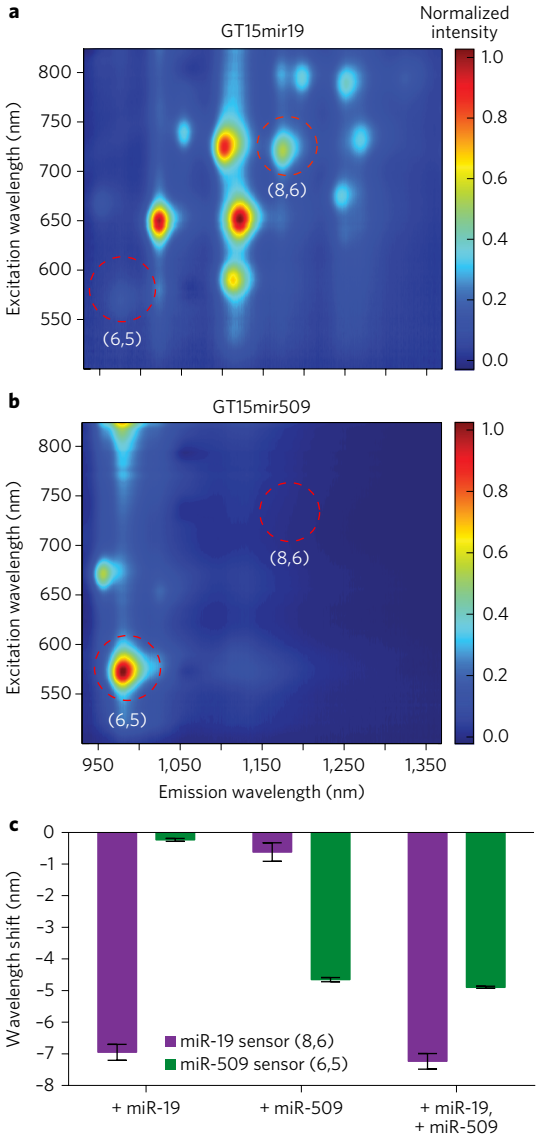


**Figure 4 | Sensor multiplexing. a**, Photoluminescence excitation/emission plot of the GT15mir19 sensor synthesized using a large-diameter nanotube preparation. **b**, Photoluminescence excitation/emission plot of the GT15mir509 sensor synthesized using a small-diameter preparation of carbon nanotubes. Red circles highlight differences in chiralities. **c**, Responses of the two sensors mixed together, on introducing miR-19 alone, miR-509 alone, or both analytes simultaneously. Error bars represent the standard deviation for three technical replicates.

introduced concomitantly into whole urine from five healthy donors and then miR-19 RNA was added. The wavelength shift response was clearly detectable against controls down to 1 nM of miRNA, and the intensity-enhancement response was similarly sensitive, at between 1 and 10 nM (Fig. 6a,b and Supplementary Fig. 33). Variation from sample-to-sample was minimal. In whole serum, we found that target miR-19 DNA was similarly detectable in the presence of SDBS (Supplementary Fig 34). When target miR-19 RNA was introduced to the sensor, we found only a small response at the highest tested concentration (Supplementary Fig 34). We hypothesized that the RNA detection was complicated by RNases in the serum, which might degrade the analyte sequence, as reported elsewhere for synthetic RNA sequences[45]. We therefore added proteinase K to the serum; this is a detergent-stable protease used to deactivate RNase. Introduction of proteinase K allowed for detection

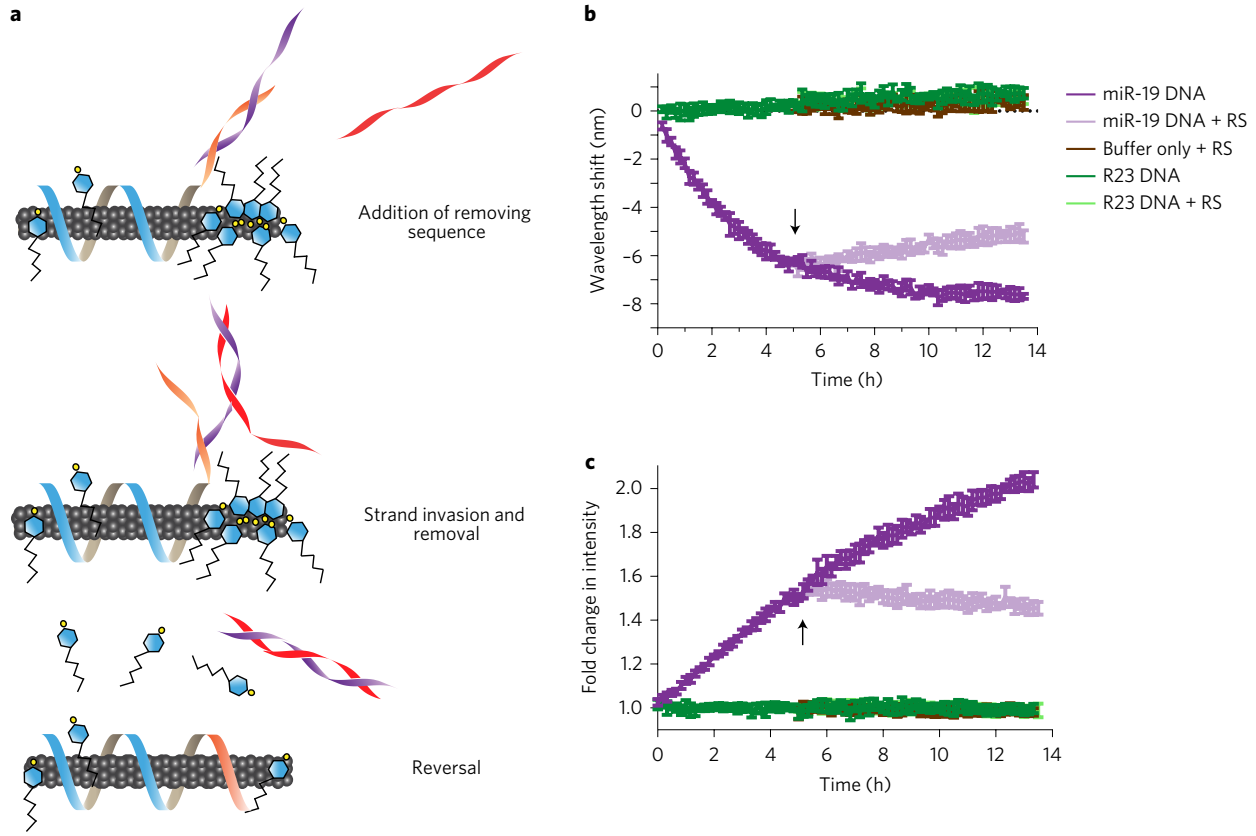


**Figure 5 | Monitoring toehold-mediated strand displacement. a**, Cartoon depicting the experiment, wherein the GT15mir19 sensor contains a truncated miRNA-capture sequence (orange domain). On hybridization with miR-19, a six-nucleotide toehold remains on the miRNA sequence (purple strand). The removing strand (red), which is complementary to the entire miRNA sequence, is introduced to remove miR-19. **b**,**c**, Kinetics of the wavelength (**b**) and intensity (**c**) responses of the GT15mir19 sensor on addition of the target miRNA sequence, and after subsequent addition of the removing strand (RS) at the time denoted by the arrow. Error bars represent the standard deviation for three technical replicates.

of miR-19 RNA with the same sensitivity as for the DNA analogue (Fig. 6c and Supplementary Fig. 34). When proteinase K was added 12 h after mixing miR-19 with the serum, the sensitivity of the response to miR-19 RNA was not improved, suggesting that the RNA had been destroyed. To verify the broad applicability of this method, we also used miR-21 as a target, due to its significance as a serum colorectal cancer biomarker[46]. We similarly tested the GT15mir21 sensor in whole serum treated with proteinase K and found that miR-21 RNA could be detected directly in minimally treated serum via both blue-shifting and intensity enhancement (Fig. 6c and Supplementary Fig. 35).

**Detection of miRNA *in vivo*.** We explored the potential of the sensor to detect miRNA *in vivo* via a minimally invasive implantable device. We loaded the SDBS-treated GT15mir19 sensor into a semipermeable membrane capillary with a molecular weight cut-off of 500 kDa (Fig. 6d). To determine whether this cut-off would prevent the diffusion of the GT15mir19 sensor complexes outside of the membrane, we calculated the molecular weight of the GT15mir19 sensor. We estimated that the sensor complexes with the narrowest diameter (0.8 nm) and an average length of 166 nm were in the range of 701 to 839 kDa (see Supplementary Text). We surmised that the miR-19 miRNA, with a molecular weight of 7.055 kDa, would pass through the membrane.

We also assessed the likelihood that the enhanced signal response provided by SDBS would continue after device implantation. We thus filled the semipermeable capillary with SDBS-pretreated GT15mir19 sensor and placed it in buffer dialysate for 6 h. The buffer was changed and the sensor response was assessed every 2 h using miR-19 (Supplementary Fig. 36). We found that the GT15mir19 sensor exhibited a nearly identical blue-shift response after 6 h of dialysis, suggesting that the SDBS remained associated with the sensor even under these conditions.

We tested the sensor response *in vivo* after surgically implanting the membrane into the peritoneal cavity of NU/J (nude) mice. The membrane was placed medially over the intestines and sutured to the parietal peritoneum to immobilize the device. We first tested whether DNA could be detected intraperitoneally by injecting 1 nmol of miR-19 DNA, R23 or the vehicle control. The mice exhibited no obvious adverse effects or changes in behaviour following the implantation or injection. After 90 min, the mice were anaesthetized using isofluorane. A fibre optic-based probe system was developed to excite a 0.8 $cm^2$ area with a 730 nm continuous wave laser (Fig. 6e), collect the emitted near-infrared light through the same fibre bundle, disperse the light with a Czerny-Turner spectrograph, and detect the light via a one-dimensional InGaAs array (Fig. 6f). Using the nanotube emission signal collected from the mouse, we found that the target miR-19 DNA exhibited a significant blue-shift response versus controls (Fig. 6g). The experiment was repeated using the RNA version of the analyte, resulting in a similar response (Supplementary Fig. 37). We tested the implantable device *in vitro* by immersing the filled capillary into buffer containing RNA, finding that the detection threshold was below 10 pmol (Supplementary Fig. 38). To determine the limit of detection *in vivo*, we intraperitoneally injected 50, 100 or 500 pmol of miR-19 RNA into mice implanted with the devices. After 120 min, significant wavelength shift responses were measured down to 100 pmol (Fig. 6h). The devices were removed

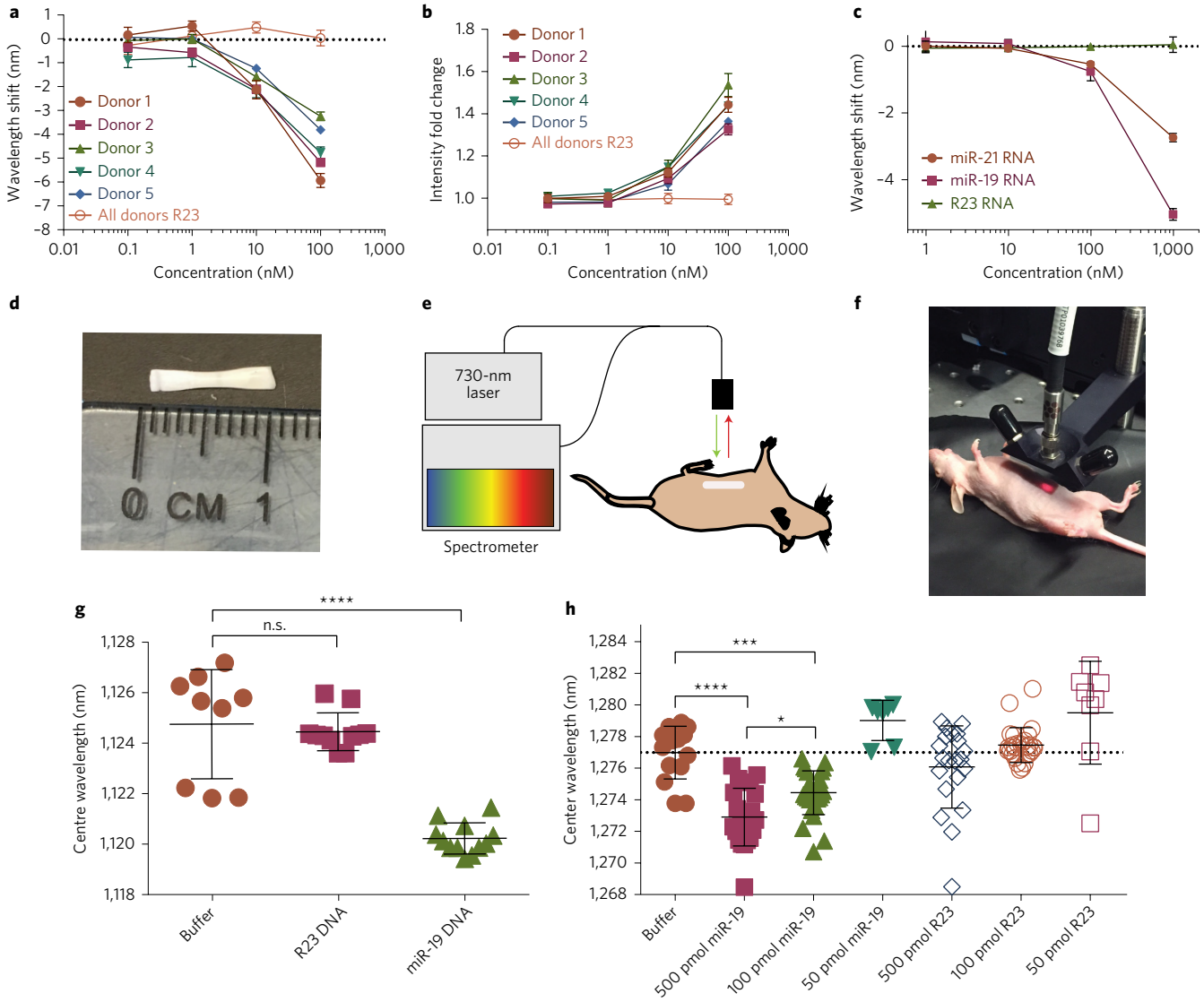


**Figure 6 | Detection of miRNA in biofluids and non-invasively in live mice. a**, Response of the emission wavelength of the GT15mir19 sensor ((7,6) nanotubes) to miR-19 spiked into urine from five healthy donors. 'All donors R23' is the average of the five donors at each concentration tested. **b**, Intensity response of the sensor in urine. **c**, Wavelength response of the nanotube sensor complex to miR-21 and miR-19 miRNA in foetal bovine serum. Error bars in **a**–**c** represent the standard deviation of three technical replicates. **d**, Semipermeable membrane encapsulating the GT15mir19 sensor for implantation. **e**, Diagram of near-infrared probe apparatus for illuminating and measuring the sensor response *in vivo*. **f**, Image of the near-infrared probe system measuring the nanotube response in a live mouse. **g**, Response of the implanted sensor ((9,4) nanotubes) device to miR-19 DNA in live mice (3–4 measurements per mouse; 3 mice per group). Error bars represent the standard deviation within each treatment group ($n=3$), and the line between them represents the mean. A one-way ordinary analysis of variance was used to compare the mean of each group to that of the buffer control. Statistical significance was calculated via Dunnet's multiple comparison test. $^{****}P<0.0001$; n.s., not significant. **h**, Response of implanted sensor ((8,7) nanotubes) device to 500, 100 and 50 pmol of miR-19 RNA or R23 RNA injected intraperitoneally into mice (3–4 measurements per mouse; 3 mice per group). R23 (50 pmol) was slightly red-shifted compared with the buffer-control. The dotted line represents the mean of the buffer-only group. Error bars and statistical analyses are as for **g**, with the addition of a Sidak's multiple comparison test to compare the miR-19 groups ($\alpha=0.05$). $^{****}P<0.0001$; $^{***}P<0.001$; $^{*}P<0.05$.

from the animals and measured *ex vivo*, producing similar results (Supplementary Fig. 39). We suspect that the detection limit was higher *in vivo* than *in vitro* because of miRNA degradation occurring in the peritoneal fluid, as well as fluid exchange out of the peritoneal cavity. The measurement of endogenous miRNA targets, which are highly stable due in part to their association with proteins such as argonaute 2[47,48], may help improve sensor performance in future investigations.

## Outlook

We engineered a label-free, amplification-free optical sensor for the quantitative detection of oligonucleotide hybridization events *in vitro* and non-invasively *in vivo*. The sensor mechanism, based on competitive displacement of both electrostatic charge and water from the carbon nanotube surface, has implications for the improvement of carbon-nanotube-based optical and electronic sensors. We also gained a clear understanding of the effects of length, mismatches in sequence and orientation of longer oligonucleotides on the optical response of the carbon nanotube, providing a basis for continued optimization. The GT15mirX sensor enabled detection via single-molecule sensor elements and multiplexing using multiple nanotube chiralities. The monitoring of toehold-based strand displacement events portends use in nucleic acid-based logic circuits[49] and also allowed the reversal of the sensor response

and regeneration of the sensor complex, which may potentially be exploited for continuous use.

For the current iteration of the sensor, *in vitro* applications such as point-of-care diagnostics may provide the most immediate route to clinical use. We found that the sensor can directly detect oligonucleotides in heterogeneous biofluids such as urine and serum with minimal pre-treatment, potentially circumventing biases and variability related to typical pre-analytical steps required for reverse-transcription qPCR[38]. Regarding sensor parameters pertinent to clinical measurements, a survey of the miRNA content in 12 body fluids[8] provided useful quantitative information to estimate the physiological range of miRNA. In urine, the median concentration of a miRNA species is on the order of tens of pM[8], while in plasma and peritoneal fluid it is in the hundreds of pM[8]. Other quantitative sensors[50] found biofluid miRNA concentrations in the high femtomolar range, suggesting that the dynamic range may be about 10 fM to 100 pM. The current detection limit for the sensor in bulk solution is in the picomolar range, although the detection threshold and dynamic range depend on several factors, including binding-site coverage, that have not yet been modulated in the development/testing process. We also demonstrated the ability to measure single-nanotube responses representing the binding of 1–60 miRNA copies, suggesting developments that might attain sensitivities down to tens of miRNA molecules, potentially rivalling the most sensitive techniques[45,51,52].

An implantable optical sensor device for the non-invasive detection of biomarkers such as miRNA may potentially be used in conjunction with wearable devices to facilitate optical readout and data recording. Our sensor implant quantified miRNA down to 100 pmol *in vivo*, although further optimization of the sensitivity and other parameters is warranted. While *in vitro* experiments suggest the current version of the sensor to be robust over at least several hours, more testing is needed to determine stability over longer periods. Investigations are also needed to ensure that oligonucleotides can be detected in their physiological states. For example, miRNA is often found associated with the small protein argonaute 2 (ref. [47]), which makes it physiologically stable. Functionally, argonaute 2 binds to miRNA in a conformation to favour hybridization with target sequences, especially over an eight nucleotide section called the seed sequence[53,54], but steric hindrance or charge interactions of the protein with miRNA could slow access to the protein-bound sections of the strand. Future iterations of a sensor may include locked nucleic acids[55] or peptide nucleic acids[56] to enhance binding affinities to short, unbound sections of miRNA. Future studies are also needed to investigate device form factors for implantation and data collection strategies, such as sensor interrogation using wearable devices.

## Methods

**DNA suspension of carbon nanotubes.** Carbon nanotubes produced by the HiPco process (Unidym), CoMoCAT process (SG65i grade, Sigma) or a combustion process (APT-200, Nano-C) were mixed with DNA oligonucleotides (IDT DNA) at a 2:1 mass ratio in 1 ml of saline-sodium citrate (SSC) buffer (G Biosciences) and ultrasonicated for 30 min at 40% amplitude (Sonics & Materials). The complete list of DNA sequences used for the suspensions can be found in the Supplementary Methods. Following ultrasonication, the dispersions were ultracentrifuged (Sorvall Discovery 90SE) for 30 min at 280,000 *g*. The top 80% of the supernatant was collected. Absorbance spectra were acquired using an ultraviolet/visible/near infrared spectrophotometer (Jasco V-670). The concentration was calculated using the extinction coefficient, $Abs_{910} = 0.02554 l\,mg^{-1}\,cm^{-1}$; where $l$ is the path length. To remove free DNA, 100 kDa Amicon centrifuge filters (Millipore) were used. The DNA–nanotube complexes were re-suspended in SSC.

**Fluorescence spectroscopy of carbon nanotubes in solution.** Fluorescence emission spectra from aqueous nanotube solutions were acquired using a home-built apparatus consisting of a tunable white light laser source, inverted microscope and InGaAs near-infrared detector. The SuperK EXTREME supercontinuum white light laser source (NKT Photonics) was used with a VARIA variable bandpass filter accessory capable of tuning the output from 500 to 825 nm with a bandwidth of 20 nm. The light path was shaped and fed into the back of an inverted IX-71 microscope (Olympus) where it passed through a ×20 near-infrared objective (Olympus) and illuminated a 50–100 µl nanotube sample in a 96-well plate (Corning). The emission from the nanotube sample was collected through the ×20 objective and passed through a dichroic mirror (875 nm cut-off; Semrock). The light was f-number matched to the spectrometer using several lenses and injected into an Isoplane spectrograph (Princeton Instruments) with a slit width of 410 µm which dispersed the emission using a 86 g mm$^{-1}$ grating with a 950 nm blaze wavelength. The spectral range was 930–1,369 nm with a resolution of ~0.7 nm. The light was collected by a PIoNIR InGaAs 640 pixel × 512 pixel array (Princeton Instruments). A HL-3-CAL-EXT halogen calibration light source (Ocean Optics) was used to correct for wavelength-dependent artefacts in the emission intensity arising from the spectrometer, detector and other optics. A Hg/Ne pencil style calibration lamp (Newport) was used to calibrate the spectrometer wavelength. Background subtraction was conducted using a well in a 96-well plate filled with deionized= water. Following acquisition, the data was processed using custom code written in MATLAB (R2014a; MathWorks), which applied the aforementioned spectral corrections and background subtraction, and was used to fit the data with Lorentzian functions.

**Atomic force microscopy.** The GT15mir19 sensor was incubated overnight at 20 mg l$^{-1}$ with 10 µM of the miR-19 hairpin or 10 µM of the R23 hairpin in SSC diluted 20-fold in 20 mM HEPES + 5 mM $MgCl_2$. The sample was plated on a freshly cleaved mica substrate (SPI) for 4 min before washing with 10 ml of distilled water and blowing dry with argon gas. An Asylum Research MFP-3D-Bio instrument was used with an Olympus AC240TS AFM probe in alternating-current mode. Data was captured at 2.93 nm pixel$^{-1}$ $x$–$y$ resolution and 15.63 pm $z$ resolution. For AFM under aqueous conditions, 20 mg l$^{-1}$ of the GT15mir19 sensor was incubated overnight with 10 µM of the miR-19 hairpin, R23 hairpin or buffer. All three conditions were spin-filtered three times with 100 kDa Amicon centrifuge filters, and resuspended with 5 mM $NiCl_2$ in 20 mM HEPES buffer (pH 6.7). The samples were plated onto freshly cleaved mica for 2 min before being gently washed with the same buffer. Samples were imaged in a droplet of the buffer using an Asylum Research Cypher ES + BlueDrive AFM with an Olympus AC55 probe and imaged using BlueDrive excitation at the ambient temperature in the AFM enclosure (31 C°). The three samples were imaged consecutively using the same probe and scan settings, starting with the miR-19-hairpin sample, followed by the R23-hairpin control and the buffer control.

**Hybridization experiments in buffers and biofluids.** Hybridization experiments were conducted with 2 mg l$^{-1}$ of the GT15mir19 sensor in SSC buffer at room temperature. Target DNA or RNA was introduced to reach a final concentration of 1 µM. Samples were incubated for 4 h, unless otherwise stated. Free energy of hybridization was predicted using OligoAnalyzer v.3.1 (IDT). Kinetics experiments were measured every 10 min using custom LabView code. Hybridization experiments with SDBS were conducted at a final concentration of 0.2% w/v. SDBS was added to the GT15mir19 sensor and allowed to equilibrate overnight at room temperature before target oligonucleotides were added. Toehold-mediated strand displacement experiments were performed with 1 µM of target miR-19 DNA and 10 µM of the removing strand, composed of a single-stranded DNA oligonucleotide with the complementary sequence to miR-19. Hybridization experiments in urine were conducted in samples from five healthy volunteers and stored on ice until the experiment. Concentrated GT15mir19 was added to each sample at a final concentration of 0.2 mg l$^{-1}$, and SDBS was added at 0.2%. Concentrated DNA and RNA targets were added at the concentrations indicated in Fig. 6a and incubated at room temperature overnight. Serum experiments used foetal bovine serum (Life Sciences) with GT15mir19 added at a final concentration of 0.2 mg l$^{-1}$ and SDBS at 0.2%. Where indicated, proteinase K (New England Biolabs) was added at 0.5 mg ml$^{-1}$. Spectra were acquired after overnight incubation at room temperature.

**Single-nanotube measurements.** Single-nanotube measurements were performed by incubating SDS-treated GT15mir19 sensors (0.2% SDS in SSC buffer) on a poly-D-lysine coated glass bottom plate (Mattek) for 10 min before gentle washing with 0.2% SDS in SSC buffer. A 1 ml volume of SDS-buffer was left in the plate during hyperspectral imaging measurements of the surface-bound nanotubes. A small volume (1 µl) of 1 mM solutions of miR-19 RNA or R23 RNA were then mixed with the buffer. Hyperspectral imaging measurements were repeated after 15 and 50 min. Single-nanotube emission spectra were collected via a custom near-infrared hyperspectral microscope, as described previously[29]. Data was processed using ImageJ[57]. Peaks were fit to Lorentzian functions using custom MATLAB code to obtain centre wavelength values.

**Molecular dynamics simulations.** MD simulations were conducted using the (9,4) nanotube chirality in explicit water. The DNA molecule for GT15mir19 (without complementary strand) was generated as an unstructured single-stranded DNA and placed near the (9,4) nanotube, followed by a sufficiently long equilibration MD simulation enhanced with a replica-exchange based method[58,59] to let the entire strand adsorb onto the (9,4) nanotube surface. Analysis of an additional 250-ns-long MD simulation is presented in the results. The DNA molecule for GT15mir19 hybridized with the complementary strand was created in a partially double-stranded form. miR-19 was generated in the double-stranded form

using the NAB program of AmberTools[60] and was appropriately bonded via phosphodiester bonds to the single-stranded $(GT)_{15}$ segment of the GT15mir19 DNA. The single-stranded $(GT)_{15}$ nanotube binding portion was adsorbed to the nanotube. The entire DNA and nanotube construct was solvated in a 10.65 nm × 10.65 nm × 14.7179 nm water-box containing approximately 55,000 water molecules and 74 sodium counterions, placed randomly, to balance the negative charges from phosphates on the DNA. The total system was approximately 170,000 atoms. The nanotube extended to the edges of the water-box and was kept frozen in place during the entire equilibration and simulation time. The nanotube atoms were modelled as $sp^2$ hybridized carbon. All structures were visualized in VMD[61].

The Gromacs (v.4.6.7) simulation package[62,63] was used with the Charmm36/TIP3P nucleic acid/water model[64]. Long-range electrostatics were calculated using the particle mesh Ewald method with a 0.9 nm real space cut-off[65]. For van der Waals interactions, a cut-off value of 1.2 nm was used. The energy-minimized simulation box was then subjected to a 100 ps equilibration in an NVT ($T = 300$ K) ensemble where the number of water molecules were fine-tuned to make average pressure approximately equivalent to atmospheric pressure. Further equilibration runs were performed for 100–200 ns in the NVT ($T = 300$ K) ensemble. The video and analysis used the 250 ns production run, followed by equilibration. Systems were propagated using stochastic Langevin dynamics with a time step of 2 fs. The trajectories were saved every 10 ps, yielding a total of 25,000 snapshots for production analysis. VMD Movie Maker was used to create the movie of the trajectory. Custom python scripts calling the MDAnalysis module[66] were used for all other analyses presented.

**Quantification of DNA on the nanotube complex.** The GT15mir19 sequence was used to suspend nanotubes as described earlier. After each of four centrifugation filter steps using the Amicon centrifuge filter (molecular weight cut-off, 100 kDa), the concentration of the filtered DNA was measured using $Abs_{260}$ on a NanoDrop spectrophotometer (Thermo Fisher). The pellet from centrifugation was also filtered to measure free DNA. The final mass of DNA from the combined values was calculated from the concentration and subtracted from the initial value. From three suspensions, we found that $3.5 \pm 1.8$ mg of DNA suspended 1 mg of nanotube, matching previous reports of 2.5–5.0 mg of DNA per 1 mg of nanotube[67].

**Device implantation and *in vivo* spectroscopy.** All animal experiments were approved by the Institutional Animal Care and Use Committee at Memorial Sloan Kettering Cancer Center. KrosFlo implant membranes (molecular weight cut-off, 500 kDa) were obtained from Spectrum Labs. The membrane was cut to about 1 cm in length and filled with approximately 15 µl of 2 mg $l^{-1}$ GT15mir19-nanotubes. Each end was heat sealed. A total of 36 NU/J (nude) mice (Jackson Labs) were anaesthetized with 2% isoflurane and implanted with the membrane. Nine mice were divided into three cohorts of three mice to receive miR-19 DNA, R23 DNA or buffer vehicle via an intraperitoneal injection of 1 nmol in 1 ml of SSC. An identical experiment was performed with miR-19 RNA, R23 RNA or buffer vehicle at 1 nmol, 500 pmol, 100 pmol or 50 pmol in 1 ml of SSC. The mice were removed from anaesthesia and allowed to regain consciousness. After 90 or 120 min, mice were anaesthetized and measured using a custom-built reflectance-probe-based spectroscopy system. The system consisted of a continuous-wave 1 W, 730 nm diode laser (Frankfurt). The laser light was injected into a bifurcated fibre optic reflection probe bundle. The sample leg of the bundle included one fibre optic cable for sample excitation at the centre of another six fibre optic cables for collection of the emitted light; the diameters and numerical apertures of the cables were 200 µm and 0.22, respectively. Emission below 1,050 nm was filtered using longpass filters, and the light was focused into the slit of a Czerny-Turner spectrograph with a 303 mm focal length (Shamrock 303i, Andor). The slit width of the spectrograph was set at 410 µm. The light was dispersed using an 85 g $mm^{-1}$ grating with a 1,350 nm blaze wavelength and collected via an iDus InGaAs camera (Andor). Spectra were fit to Voigt functions using custom MATLAB code.

**Code availability.** The custom MATLAB code is available from the authors on request.

**Data availability.** The authors declare that all data supporting the findings of this study are available within the paper and its Supplementary Information. Source data for the figures in this study are available in *figshare* with the identifier http://dx.doi.org/10.6084/m9.figshare.4567945 (ref. [68]).

Received 10 August 2016; accepted 27 January 2017; published 13 March 2017

## References


1. Tokuhisa, M. *et al.* Exosomal miRNAs from peritoneum lavage fluid as potential prognostic biomarkers of peritoneal metastasis in gastric cancer. *PLoS ONE* **10,** e0130472 (2015).
2. Parrella, P., Zangen, R., Sidransky, D. & Nicol, T. Molecular analysis of peritoneal fluid in ovarian cancer patients. *Mod. Pathol.* **16,** 636–640 (2003).
3. Mitchell, P. S. *et al.* Circulating microRNAs as stable blood-based markers for cancer detection. *Proc. Natl Acad. Sci. USA* **105,** 10513–10518 (2008).
4. Dawson, S. J. *et al.* Analysis of circulating tumor DNA to monitor metastatic breast cancer. *N. Engl. J. Med.* **368,** 1199–1209 (2013).
5. Tomlins, S. A. *et al.* Urine TMPRSS2:ERG fusion transcript stratifies prostate cancer risk in men with elevated serum PSA. *Sci. Transl. Med.* **3,** 94ra72 (2011).
6. Thierry, A. R. *et al.* Clinical validation of the detection of KRAS and BRAF mutations from circulating tumor DNA. *Nat. Med.* **20,** 430–435 (2014).
7. Deras, I. L. *et al.* PCA3: a molecular urine assay for predicting prostate biopsy outcome. *J. Urol.* **179,** 1587–1592 (2008).
8. Weber, J. A. *et al.* The microRNA spectrum in 12 body fluids. *Clin. Chem.* **56,** 1733–1741 (2010).
9. Lawrie, C. H. *et al.* Detection of elevated levels of tumour-associated microRNAs in serum of patients with diffuse large B-cell lymphoma. *Br. J. Haematol.* **141,** 672–675 (2008).
10. Yamada, Y. *et al.* MiR-96 and miR-183 detection in urine serve as potential tumor markers of urothelial carcinoma: correlation with stage and grade, and comparison with urinary cytology. *Cancer Sci.* **102,** 522–529 (2011).
11. Hanke, M. *et al.* A robust methodology to study urine microRNA as tumor marker: microRNA-126 and microRNA-182 are related to urinary bladder cancer. *Urol. Oncol.* **28,** 655–661 (2010).
12. Snowdon, J., Boag, S., Feilotter, H., Izard, J. & Siemens, R. A pilot study of urinary microRNA as a biomarker for urothelial cancer. *Can. Urol. Assoc. J.* **7,** 28–32 (2013).
13. Lan, Y. F. *et al.* MicroRNA-494 reduces ATF3 expression and promotes AKI. *J. Am. Soc. Nephrol.* **23,** 2012–2023 (2012).
14. Chung, Y. W. *et al.* Detection of microRNA as novel biomarkers of epithelial ovarian cancer from the serum of ovarian cancer patient. *Int. J. Gynecol. Cancer* **23,** 673–679 (2013).
15. Pajek, J. *et al.* Cell-free DNA in the peritoneal effluent of peritoneal dialysis solutions. *Ther. Apher. Dial.* **14,** 20–26 (2010).
16. Johnson, B. N. & Mutharasan, R. Biosensor-based microRNA detection: techniques, design, performance, and challenges. *Analyst* **139,** 1576–1588 (2014).
17. Chen, C. *et al.* Real-time quantification of microRNAs by stem-loop RT-PCR. *Nucleic Acids Res.* **33,** e179 (2005).
18. Baker, M. MicroRNA profiling: separating signal from noise. *Nat. Methods* **7,** 687–692 (2010).
19. Hunt, E. A., Broyles, D., Head, T. & Deo, S. K. MicroRNA detection: current technology and research strategies. *Annu. Rev. Anal. Chem.* **8,** 217–237 (2015).
20. Dong, H. *et al.* MicroRNA: function, detection, and bioanalysis. *Chem. Rev.* **113,** 6207–6233 (2013).
21. Kruss, S. *et al.* Carbon nanotubes as optical biomedical sensors. *Adv. Drug Deliv. Rev.* **65,** 1933–1950 (2013).
22. Iverson, N. M. *et al. In vivo* biosensing via tissue-localizable near-infrared-fluorescent single-walled carbon nanotubes. *Nat. Nanotech.* **8,** 873–880 (2013).
23. Wang, F., Dukovic, G., Brus, L. E. & Heinz, T. F. The optical resonances in carbon nanotubes arise from excitons. *Science* **308,** 838–841 (2005).
24. O'Connell, M. J. *et al.* Band gap fluorescence from individual single-walled carbon nanotubes. *Science* **297,** 593–596 (2002).
25. Cheong, W. F., Prahl, S. A. & Welch, A. J. A review of the optical properties of biological tissues. *IEEE J. Sel. Top. Quantum* **26,** 2166–2185 (1990).
26. Heller, D. A. *et al.* Optical detection of DNA conformational polymorphism on single-walled carbon nanotubes. *Science* **311,** 508–511 (2006).
27. Barone, P. W., Baik, S., Heller, D. A. & Strano, M. S. Near-infrared optical sensors based on single-walled carbon nanotubes. *Nat. Mater.* **4,** 86–92 (2005).
28. Cognet, L. *et al.* Stepwise quenching of exciton fluorescence in carbon nanotubes by single-molecule reactions. *Science* **316,** 1465–1468 (2007).
29. Roxbury, D. *et al.* Hyperspectral microscopy of near-infrared fluorescence enables 17-chirality carbon nanotube imaging. *Sci. Rep.* **5,** 14167 (2015).
30. Olive, V. *et al.* miR-19 is a key oncogenic component of mir-17-92. *Genes Dev.* **23,** 2839–2849 (2009).
31. Zheng, M. *et al.* Structure-based carbon nanotube sorting by sequence-dependent DNA assembly. *Science* **302,** 1545–1548 (2003).
32. Bachilo, S. M. *et al.* Structure-assigned optical spectra of single-walled carbon nanotubes. *Science* **298,** 2361–2366 (2002).
33. Campbell, J. F., Tessmer, I., Thorp, H. H. & Erie, D. A. Atomic force microscopy studies of DNA-wrapped carbon nanotube structure and binding to quantum dots. *J. Am. Chem. Soc.* **130,** 10648–10655 (2008).
34. Roxbury, D., Jena, P. V., Shamay, Y., Horoszko, C. P. & Heller, D. A. Cell membrane proteins modulate the carbon nanotube optical bandgap via surface charge accumulation. *ACS Nano* **10,** 499–506 (2016).
35. Yang, R. *et al.* Carbon nanotube-quenched fluorescent oligonucleotides: probes that fluoresce upon hybridization. *J. Am. Chem. Soc.* **130,** 8351–8358 (2008).
36. Heller, D. A. *et al.* Peptide secondary structure modulates single-walled carbon nanotube fluorescence as a chaperone sensor for nitroaromatics. *Proc. Natl Acad. Sci. USA* **108,** 8544–8549 (2011).

37. Moore, V. C. *et al.* Individually suspended single-walled carbon nanotubes in various surfactants. *Nano Lett.* **3,** 1379–1382 (2003).
38. McDonald, J. S., Milosevic, D., Reddi, H. V., Grebe, S. K. & Algeciras-Schimnich, A. Analysis of circulating microRNA: preanalytical and analytical challenges. *Clin. Chem.* **57,** 833–840 (2011).
39. Gregory, P. A. *et al.* The miR-200 family and miR-205 regulate epithelial to mesenchymal transition by targeting ZEB1 and SIP1. *Nat. Cell Biol.* **10,** 593–601 (2008).
40. Landry, M. P. *et al.* Comparative dynamics and sequence dependence of DNA and RNA binding to single walled carbon nanotubes. *J. Phys. Chem. C* **119,** 10048–10058 (2015).
41. Johnson, R. R., Johnson, A. T. & Klein, M. L. The nature of DNA-base-carbon-nanotube interactions. *Small* **6,** 31–34 (2010).
42. Cognet, L., Tsyboulski, D. A. & Weisman, R. B. Subdiffraction far-field imaging of luminescent single-walled carbon nanotubes. *Nano Lett.* **8,** 749–753 (2008).
43. Machinek, R. R., Ouldridge, T. E., Haley, N. E., Bath, J. & Turberfield, A. J. Programmable energy landscapes for kinetic control of DNA strand displacement. *Nat. Commun.* **5,** 5324 (2014).
44. Srinivas, N. *et al.* On the biophysics and kinetics of toehold-mediated DNA strand displacement. *Nucleic Acids Res.* **41,** 10641–10658 (2013).
45. Johnson-Buck, A. *et al.* Kinetic fingerprinting to identify and count single nucleic acids. *Nat. Biotechnol.* **33,** 730–732 (2015).
46. Toiyama, Y. *et al.* Serum miR-21 as a diagnostic and prognostic biomarker in colorectal cancer. *J. Natl Cancer Inst.* **105,** 849–859 (2013).
47. Arroyo, J. D. *et al.* Argonaute2 complexes carry a population of circulating microRNAs independent of vesicles in human plasma. *Proc. Natl Acad. Sci. USA* **108,** 5003–5008 (2011).
48. Turchinovich, A., Weiz, L., Langheinz, A. & Burwinkel, B. Characterization of extracellular circulating microRNA. *Nucleic Acids Res.* **39,** 7223–7233 (2011).
49. Seelig, G., Soloveichik, D., Zhang, D. Y. & Winfree, E. Enzyme-free nucleic acid logic circuits. *Science* **314,** 1585–1588 (2006).
50. Joshi, G. K. *et al.* Label-free nanoplasmonic-based short noncoding RNA sensing at attomolar concentrations allows for quantitative and highly specific assay of microRNA-10b in biological fluids and circulating exosomes. *ACS Nano* **9,** 11075–11089 (2015).
51. Wanunu, M. *et al.* Rapid electronic detection of probe-specific microRNAs using thin nanopore sensors. *Nat. Nanotech.* **5,** 807–814 (2010).
52. Gunnarsson, A., Jonsson, P., Marie, R., Tegenfeldt, J. O. & Hook, F. Single-molecule detection and mismatch discrimination of unlabeled DNA targets. *Nano Lett.* **8,** 183–188 (2008).
53. Schirle, N. T. & MacRae, I. J. The crystal structure of human Argonaute2. *Science* **336,** 1037–1040 (2012).
54. Schirle, N. T., Sheu-Gruttadauria, J. & MacRae, I. J. Structural basis for microRNA targeting. *Science* **346,** 608–613 (2014).
55. Koshkin, A. A. *et al.* LNA (locked nucleic acids): synthesis of the adenine, cytosine, guanine, 5-methylcytosine, thymine and uracil bicyclonucleoside monomers, oligomerisation, and unprecedented nucleic acid recognition. *Tetrahedron* **54,** 3607–3630 (1998).
56. Nielsen, P. E., Egholm, M., Berg, R. H. & Buchardt, O. Sequence-selective recognition of DNA by strand displacement with a thymine-substituted polyamide. *Science* **254,** 1497–1500 (1991).
57. Schneider, C. A., Rasband, W. S. & Eliceiri, K. W. NIH Image to ImageJ: 25 years of image analysis. *Nat. Methods* **9,** 671–675 (2012).
58. Sugita, Y. & Okamoto, Y. Replica-exchange molecular dynamics method for protein folding. *Chem. Phys. Lett.* **314,** 141–151 (1999).
59. Bonomi, M. & Parrinello, M. Enhanced sampling in the well-tempered ensemble. *Phys. Rev. Lett.* **104,** 190601 (2010).
60. Case, D. A. *et al.* Amber 2016 (Univ. California, 2016).
61. Humphrey, W., Dalke, A. & Schulten, K. VMD: visual molecular dynamics. *J. Mol. Graph. Model.* **14,** 33–38 (1996).
62. Berendsen, H. J. C., Vanderspoel, D. & Vandrunen, R. Gromacs — a message-passing parallel molecular-dynamics implementation. *Comput. Phys. Commun.* **91,** 43–56 (1995).
63. Hess, B., Kutzner, C., van der Spoel, D. & Lindahl, E. GROMACS 4: algorithms for highly efficient, load-balanced, and scalable molecular simulation. *J. Chem. Theory Comput.* **4,** 435–447 (2008).
64. Hart, K. *et al.* Optimization of the CHARMM additive force field for DNA: improved treatment of the BI/BII conformational equilibrium. *J. Chem. Theory Comput.* **8,** 348–362 (2012).
65. Essmann, U. *et al.* A smooth particle mesh Ewald method. *J. Chem. Phys.* **103,** 8577–8593 (1995).
66. Michaud-Agrawal, N., Denning, E. J., Woolf, T. B. & Beckstein, O. MDAnalysis: a toolkit for the analysis of molecular dynamics simulations. *J. Comput. Chem.* **32,** 2319–2327 (2011).
67. Zheng, M. *et al.* DNA-assisted dispersion and separation of carbon nanotubes. *Nat. Mater.* **2,** 338–342 (2003).
68. Harvey, J. *et al.* Dataset for 'A carbon nanotube reporter of microRNA hybridization events *in vivo*'. *figshare* http://dx.doi.org/10.6084/m9.figshare.4567945 (2017).


## Acknowledgements

This work was supported by the US National Institutes of Health (NIH) Director's New Innovator Award (DP2-HD075698), NIH/National Cancer Institute (NCI) Cancer Center Support Grant (P30-CA008748), the Center for Molecular Imaging and Nanotechnology, the Louis V. Gerstner Jr. Young Investigator's Fund, the Experimental Therapeutics Center, the Alan and Sandra Gerry Metastasis Research Initiative, Cycle for Survival, the Frank A. Howard Scholars Program, the Honorable Tina Brozman Foundation for Ovarian Cancer Research, the Byrne Research Fund, the Anna Fuller Fund, Mr William H. Goodwin and Mrs Alice Goodwin and the Commonwealth Foundation for Cancer Research, and the Imaging and Radiation Sciences Program at Memorial Sloan Kettering Cancer Center. Molecular simulation work was performed at Lehigh University and is supported by the US Department of Energy (DOE) Office of Science, Basic Energy Sciences (BES), and Division of Material Sciences and Engineering, under award DE-SC0013979. Use of the high-performance computing capabilities of the Extreme Science and Engineering Discovery Environment (XSEDE) was supported by the US National Science Foundation under grant number TG-MCB-120014. This research also used resources of the National Energy Research Scientific Computing Center, a DOE Office of Science User Facility supported under contract no. DE-AC02-05CH11231. P.V.J. was supported by the NCI Grant NIH T32 Training Grant 2T32CA062948-21. H.A.B. was supported by a Medical Scientist Training Program grant from the National Institute of General Medical Sciences of the NIH under award number T32GM007739 to the Weill Cornell/Rockefeller/Sloan-Kettering Tri-Institutional MD-PhD Program. R.M.W. was supported by the Ovarian Cancer Research Fund Alliance (Anna Schreiber Mentored Investigator Award 370463). D.R. was supported by an American Cancer Society 2013 Roaring Fork Valley Research Fellowship and grant no. P20GM103430 from the National Institute of General Medical Sciences of the NIH. We thank the Molecular Cytology Core Facility at Memorial Sloan Kettering Cancer Center and N. Paknejad for the atomic force microscopy measurements.

## Author contributions

J.D.H., P.V.J. and D.A.H. conceived the research, designed the experiments and analysed the data. J.D.H. and H.A.B. performed the experiments. Programs to facilitate data analysis were written by P.V.J. and D.R. Molecular dynamics simulations and analysis were designed and conducted by G.H.Z., D.R. and J.M. Assistance with *in vivo* work was provided by R.M.W. The probe system for *in vivo* measurements was designed and built by T.V.G. and D.A.H. The manuscript was prepared and written by J.D.H. and D.A.H.; all authors contributed to editing the manuscript. D.A.H. supervised the project.

## Additional information

**Supplementary information** is available for this paper.

**Reprints and permissions information** is available at www.nature.com/reprints.

**Correspondence and requests for materials** should be addressed to D.A.H.

**How to cite this article:** Harvey, J. D. *et al.* A carbon nanotube reporter of microRNA hybridization events *in vivo*. *Nat. Biomed. Eng.* **1,** 0041 (2017).

## Competing interests

The authors declare no competing financial interests.